Journal of Geochemical Exploration 224 (2021) 106740

Contents lists available at ScienceDirect

Journal of Geochemical Exploration

journal homepage: www.elsevier.com/locate/gexplo

Cathodoluminescent textures and trace element signatures of hydrothermal quartz from the granite-related No. 302 uranium deposit, South China: A reconnaissance study for their genetic significances

Qing Lan [a,*], Jinrong Lin [b,*], Shanling Fu [a], Jincheng Luo [a]

[a] State Key Laboratory of Ore Deposit Geochemistry, Institute of Geochemistry, Chinese Academy of Sciences, Guiyang 550081, China
[b] Beijing Research Institute of Uranium Geology, China National Nuclear Corporation, Beijing 100029, China

ARTICLE INFO

Keywords:
Quartz
Cathodoluminescent texture
Trace elements in quartz
Precipitation mechanism
Uranium deposit

ABSTRACT

Cathodoluminescent (CL) texture and trace element signature of quartz from granite-related uranium deposit in southern China has been investigated to discuss their genetic significance. Results show that the pre-ore quartz (Q1) generally has dark and homogeneous (or slightly mottled) luminescent texture that may result from annealing of original CL textures; the *syn*-ore quartz (Q2) generally shows bright and oscillatory luminescent texture and the post-ore quartz (Q3) displays bright and homogeneous luminescence texture. LA-ICPMS analyses suggest Al, Li, K, Na and Ca are the most abundant elements in various generations of quartz and mainly occur as solid solution within the crystal lattice, in which Al can be incorporated into quartz by substituting Si in the crystal lattice, with additional cations (e.g., K, Na, Li and Ca) to keep the charge balance. The negative correlation between Ge and Al suggests that Ge may substitute Si independently due to the similar ion radius and charge. Fe and U may be incorporated into quartz in the form of micro-inclusions. The homogeneous CL texture and low concentration of trace elements indicate that the Q3 likely precipitated under stable thermodynamic conditions.

The low Ti concentration and oscillatory euhedral growth zones of CL textures suggest that *syn*-ore quartz (Q2) may have precipitated from a low-temperature hydrothermal fluid. Thus, it can be inferred that the ore-forming fluid in the No. 302 uranium deposit could be of a low-temperature hydrothermal fluid from which the quartz-pitchblende vein precipitated from, which is also supported by the results from fluid inclusion studies. The significantly large variations of Al and other trace elements concentrations in the *syn*-ore quartz were likely indicative of the large fluctuations of pH values of ore-forming fluid, probably resulting from the CO_2 effervescence or phase separation from ore-forming fluid, which further led to decomposing of uranyl carbonate complexes ($UO_2(CO_3)^{2-}$), and finally caused the uranium minerals depositing in the favorable structural traps to form the No. 302 uranium deposit. This study highlights that CL textures and trace element chemistry of quartz related to mineralization can be used to fingerprint the physical and chemical history of ore deposit formation.

1. Introduction

Quartz is one of the most abundant minerals in the crust and is the predominant gangue mineral in many types of hydrothermal ore deposits, in which quartz forms in a wide range of geologic environments under temperature between 50° and 750 °C and pressure conditions (Rusk, 2009; Götte et al., 2011). Quartz is chemically simple and relatively stable compared to most hydrothermal minerals, and is thus likely to preserve its geologic history (Rusk et al., 2008a). Since Crookes (1879) first observed the phenomenon of cathodoluminescence (CL), CL has been used in numerous petrologic studies of quartz from a variety of geologic environments (Seyedolali et al., 1997), particularly in hydrothermal ore deposits (Rusk et al., 2008a; Jourdan et al., 2009; Götte et al., 2011; Rusk, 2012; Frelinger et al., 2015; Fu et al., 2020).

Scanning electron microscope-cathodoluminescence (SEM-CL) can reveal internal textures of quartz that are invisible to traditional petrographic techniques (Götze et al., 2001; Frelinger et al., 2015; Fu et al., 2020). The CL-properties of quartz mainly depend on the physicochemical conditions during crystallization (Götze, 2000; Götte et al., 2011; Rusk, 2012; and references therein). Fluid composition, the extent

* Corresponding authors.
E-mail addresses: lanqing@mail.gyig.ac.cn (Q. Lan), Linjr86@163.com (J. Lin).

https://doi.org/10.1016/j.gexplo.2021.106740
Received 8 September 2020; Received in revised form 1 February 2021; Accepted 7 February 2021
Available online 11 February 2021
0375-6742/© 2021 Published by Elsevier B.V.

of fluid saturation with respect to quartz, pH, and temperature are considered to significantly influence the growth dynamics and trace element composition, and thus likely the CL properties of hydrothermal quartz (Götte et al., 2011). Like the CL textures, trace element abundance and distribution are also determined by variations in the physical and chemical conditions of hydrothermal fluid from which quartz precipitate. For example, the variation of Ti and Al concentrations in quartz is generally thought to reflect the fluctuations of temperature and pH of fluid that quartz precipitated (Rusk, 2009, 2012; Huang and Audétat, 2012; Breiter et al., 2017a). Since quartz precipitates throughout much of the history of hydrothermal systems, the CL textures and trace elements of quartz greatly enhance our ability to interpret the evolving physical and chemical conditions of hydrothermal fluid flow in the crust (Rusk, 2012).

Several studies show that specific CL textures and intensities are related to specific mineralization events at a deposit or even district-wide scale (Wilkinson et al., 1999; Landtwing et al., 2005; Rusk et al., 2006). Some good overviews of trace element chemistry of quartz from porphyry Cu deposits, orogenic-Au deposits, as well as low- and high-temperature hydrothermal deposits have been present (Rusk et al., 2006; Rusk et al., 2008a; Müller et al., 2010; Götte et al., 2011; Rusk, 2012; Rice et al., 2016; Breiter et al., 2017a, 2017b; Baele et al., 2019; Fu et al., 2020), but very few data have been reported on the granite-related uranium deposits (Baele et al., 2019) where abundant hydrothermal quartz associated with mineralization were observed.

In this study, we have investigated the CL textures and trace element signatures of hydrothermal quartz from the No. 302 uranium deposit in Changjiang uranium ore field, South China, with the aim to decipher the evolution of ore-forming fluid and precipitation mechanism of pitchblende.

2. Regional and deposit geology

The South China Block is made up of the Yangtze block to the northwest and the Cathaysian block to the southeast (Fig. 1A), and they were accreted together along the Jiangnan orogen during early Neoproterozoic (ca. 1.0–0.83 Ga) (Charvet, 2013 and references therein). More than 90% of the outcrop area of the eastern Cathaysian block is covered by late Mesozoic volcanic and granitic rocks (Fig. 1B; Gilder et al., 1996; Sun, 2006; Zhou, 2007). The Nanling metallogenic belt is situated within the central part of the Cathaysian Block and is dominantly covered by Mesozoic granites accompanying with abundant W, Sn, U and Nb—Ta deposits (Hu and Zhou, 2012; Mao et al., 2013, 2019; Gao et al., 2014; Hu et al., 2017), represented by the Zhuguang U ore fields (Dahlkamp, 2009) and the southern Jiangxi W—Sn metalloginc province (Legros et al., 2016). In the east-central part of the Nanling metallogenic belt, the major tectonic-magmatic reactivations occurred during the Indosinian orogeny and the Yanshanian post-orogenic event, which produced a series of composite granitic batholiths, including the Zhuguang, Guidong, Jiuyishan and Jinjiling batholiths (Dahlkamp, 2009). Most granite-related vein-type uranium deposits in this region are interpreted to have been associated with Indosinian and Yanshanian granites (Fig. 2; Dahlkamp, 2009; Deng et al., 2012; Zhang et al., 2017a).

The Changjiang uranium ore field in the northern part of Guangdong province is one of the most important granite-related uranium ore fields in South China. The U mineralization primarily occurred in the southeastern part of the Zhuguang complex that is composed of Caledonian and Indosinian granites, and Yanshanian granites and mafic dykes at the

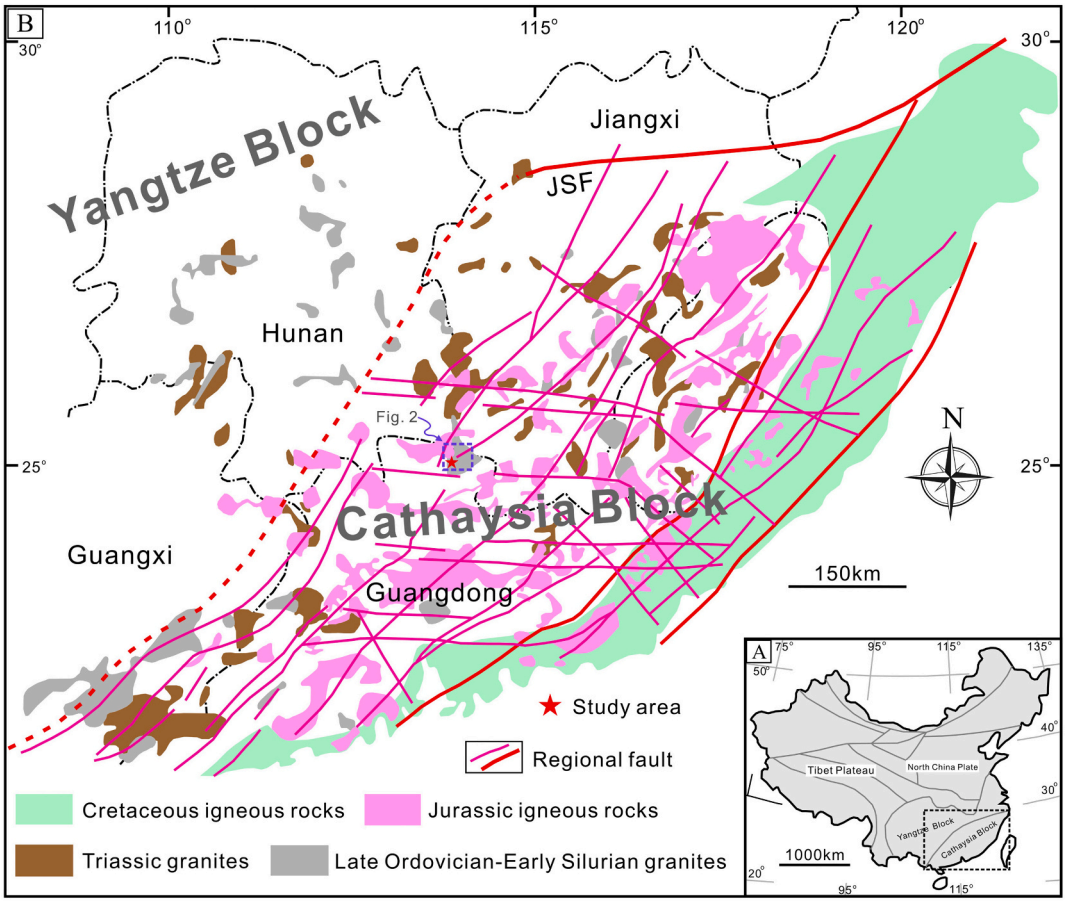

Fig. 1. A: Geological map showing the principal tectonic framework of China. B: Schematic map of the Cathaysia block showing the structure, igneous rocks and location of the studied area (modified after Sun, 2006; Li et al., 2010). JSF: Jiangshan-Shaoxing Fault.

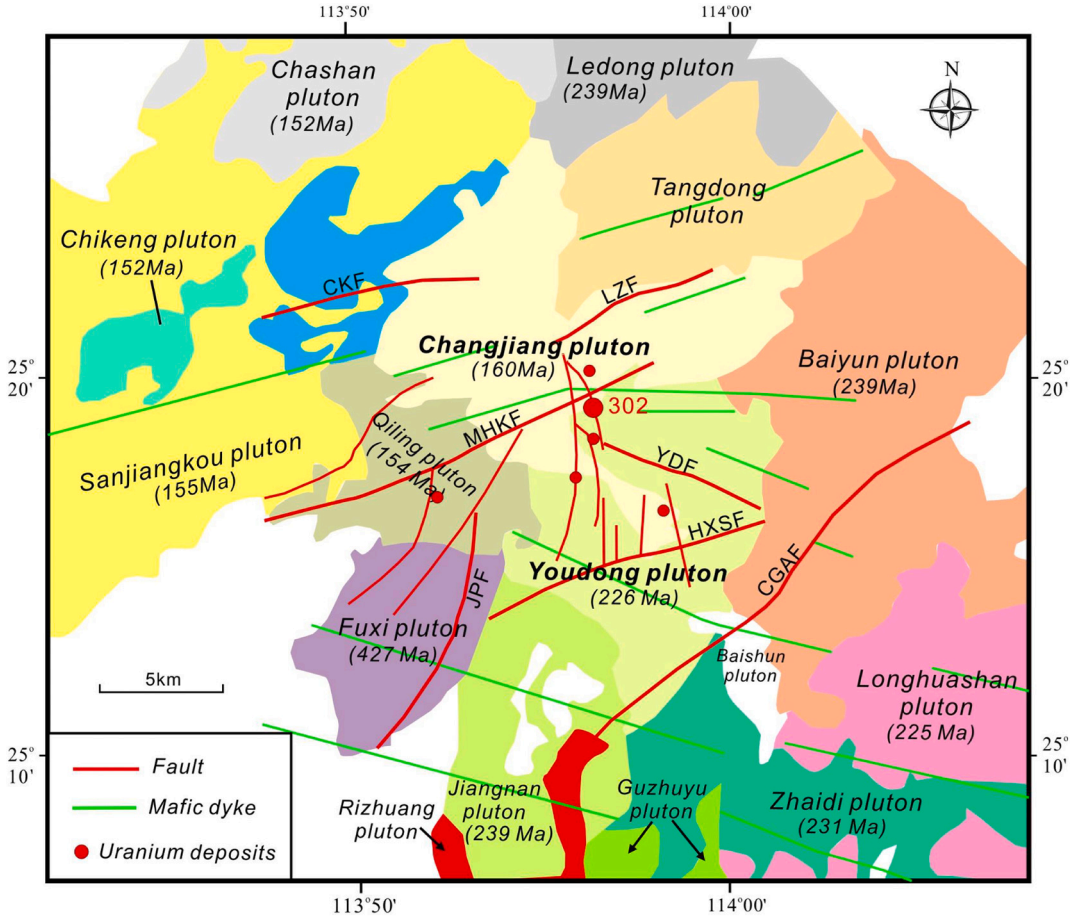

Fig. 2. Geological map of the southern Zhuguang granite massif showing the distribution of granites, structure and the uranium deposits hosted in granites (modified after Zhang et al., 2018; Zhang, 2008). CKF: Chengkou Fault; LZF: Lizhou Fault; MHKF: Mianhuakeng Fault; YDF: Youdong Fault; HXSF: Huangxishui Fault; CGAF: Chenggongao Fault; JPF: Jiaoping Fault.

juncture of northern Guangdong, southeastern Hunan and southwestern Jiangxi regions (Figs. 1, 2; Deng et al., 2011, 2012). The structures in this region mainly include NE–SW, NW–SE, N—S, and E–W striking faults (Fig. 2). Three NE–SW striking regional faults (Lizhou, Mianhuakeng, and Huangxishui faults, from north to south), and one NW–SE striking fault known as Youdong fault are the main structures and the N—S striking faults are the major ore-bearing structures.

The No. 302 uranium deposit is located in the eastern part of the Changjiang U ore field and is controlled mainly by both of the NE-trending Mianhuakeng fault and NW-trending Youdong fault (Fig. 2). The ore bodies emplaced into the contact zone between the Indosinian two-mica granite (232 ± 4 Ma) and Early Yanshanian biotite granite (the U—Pb age is 160 ± 2 Ma) (Deng et al., 2011; Huang et al., 2012, 2015). The ores commonly occur as veins or lenses of quartz-pitchblende in brecciated and altered granite (Fig. 3). The major U mineral is fine-grained pitchblende associated with microcrystalline quartz and quartz-calcite-fluorite veins (Figs. 3, 4).

The wallrock magmatic rocks in the studied area are mainly two-mica granite and biotite granite (Fig. 2). The two-mica granite is widespread in the south and east of the studied area, and generally contains xenomorphic quartz (25–30%), K-feldspar (35–40%), plagioclase (25–30%), biotite (5–8%), and muscovite (2–5%), along with accessory minerals including zircon and apatite. The biotite granite is characterized by porphyritic textures with K-feldspar phenocrysts, and its mineral composition is generally quartz (25%), K-feldspar (20%), plagioclase (30%), and biotite (20%), with minor amounts of muscovite. The main mineral species are almost similar in these two granites, although their proportions are variable (Zhang et al., 2017a, 2017b).

Based on the ore textures and paragenetic relationships of the primary minerals, three stages can be identified, namely pre-ore stage, *syn*-ore and post-ore stages (Fig. 5; Zhang et al., 2017a). The pre-ore stage quartz was formed during magmatic stage (Zhang et al., 2017a) or high-temperature quartz vein stage (Huang et al., 2015) before uranium mineralization. The syn-ore minerals are primarily quartz, pitchblende, pyrite, hematite, chlorite, hydromica, fluorite, and kaolinite, and the post-ore minerals include quartz, calcite, fluorite, pyrite, and hematite (Fig. 5). Due to the alteration of the magmatic minerals of granitic rocks resulting from the ore-forming hydrothermal fluids, the U mineralization is closely associated with silicification, pyritization, hematization and atropurpureus fluorite (Huang et al., 2015).

The pitchblende is closely associated with quartz and pyrite in the No. 302 uranium deposit. The hydrothermal mineralization veins are mainly quartz- pitchblende vein or quartz-pitchblende-pyrite vein. The quartz-pitchblende veins contain fewer inclusions than the altered granite samples (Zhang et al., 2017a). Three generations of quartz can be recognized in this deposit, namely the pre-ore, syn-ore and post-ore quartz (Fig. 5 ; Zhang et al., 2017a). The pre-ore quartz is present as fractured grains and filled with syn-ore quartz-pitchblende veins (Fig. 3F, 4A). Under cross- polarized light, the syn-ore quartz vein in No. 302 uranium deposit display microcrystalline and comb features and intergrown with pitchblende (Fig. 3). The previous study suggests that microcrystalline quartz served as the main carriers of pitchblende (Feng et al., 2009). Plane- and cross-polarized light observations under optical microscope show typical mosaics of hydrothermal quartz with little textural information to further differentiate different generations of quartz growth or to relate to specific mineralization events. The post-ore

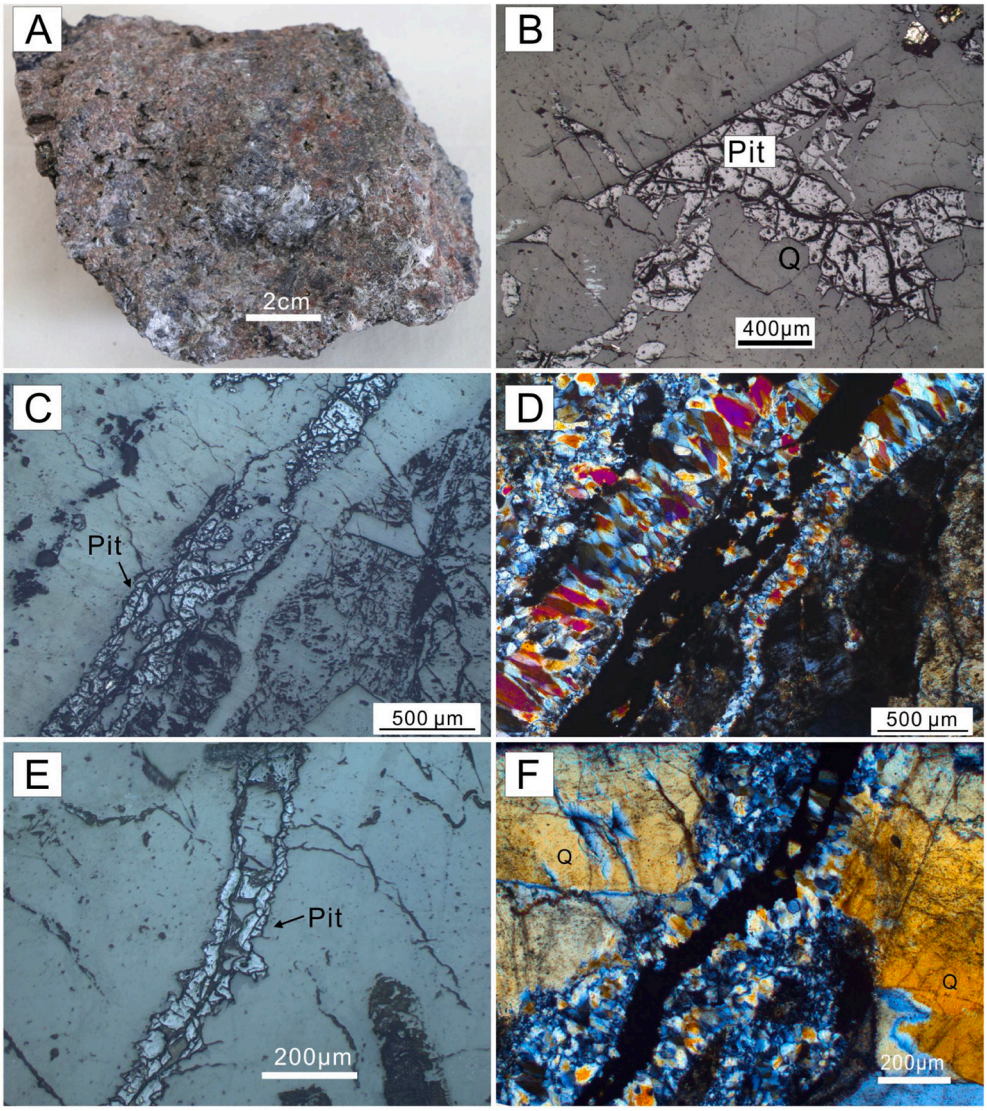

Fig. 3. Major types of mineralization in the No. 302 uranium deposit. A: the red (or pig liver color) ore. B: the pitchblende under reflected light. C: the quartz-pitchblende vein that filling the crack of altered host rock (under reflected light). D: The microcrystalline and comb quartz in quartz-pitchblende vein (under cross-polarized light). E and F: the quartz-pitchblende vein and the microcrystalline and comb quartz under reflected light (E) and cross-polarized light (F). The pre-ore quartz was observed to be yellow under cross-polarized light due to the thickened rock slice. Pit: pitchblende; Q: quartz. (For interpretation of the references to color in this figure legend, the reader is referred to the web version of this article.)

quartz is observed to cut the quartz-pitchblende vein but no pitchblende was identified in this vein (Fig. 4D).

3. Samples and analytical methods

Cathodoluminescence textures and trace element composition of quartz were studied in thin sections (60 μm thick) from 7 ore samples selected from drill cores and mining tunnels at the No. 302 uranium deposit. Petrographic observations were conducted in 5 doubly polished thin sections with the optical microscope, and some of them were selected for further analysis. The shape of quartz crystals was examined under microscope with transmitted and cross-polarized light prior to further analysis.

Scanning electron microscope-cathodoluminescence (SEM-CL) analyses of quartz were conducted on a JSM-7800F SEM equipped with a Mono CL4 detector at the State Key Laboratory of Ore Deposit Geochemistry (SKLODG), Chinese Academy of Sciences. The acceleration voltage was set at 15 kV and the probe current was ~10 nA. SEM-CL images and transmitted light images were combined to identify quartz textures and help to select the area for the subsequent LA-ICPMS analysis to avoid the fluid or mineral inclusions in quartz.

A JEOL JXA-8530F Plus EPMA was used to determine the contents of Si, Al, Ti, K, Ca, Fe and U in quartz using a beam size with a diameter of 1–10 μm and a beam current of 20 nA accelerated at 25 KeV at the SKLODG, Chinese Academy of Sciences. SiO_2, Kaersutite, UO_2 were taken as standards for the following elements: Si, Al, K, Ti, Ca, Fe, U. The precision of the analyses (at 3σ) is 420 ppm for Si, 450 ppm for Al, 460 ppm for Ti, 130 ppm for K, 135 ppm for Ca, 270 ppm for Fe and 530 ppm for U.

Trace element analyses of quartz in this study were carried out by LA-ICPMS at the SKLODG. Laser sampling was performed using the GeoLasPro 193 nm ArF excimer laser. The Agilent 7900 ICP-MS instrument was used to acquire ion-signal intensities. Laser repetition of 10 Hz, energy density of 10 J/cm^2 and laser spot size of 40 μm were used during the analyses. Helium was applied as a carrier gas which was mixed with Argon via a T-connector before entering the ICP-MS. Twenty seconds of background signal and sixty seconds of ablation were collected for each analysis spot. The following isotopes were measured including ^{7}Li, ^{23}Na, ^{27}Al, ^{39}K, ^{43}Ca, ^{85}Rb, ^{49}Ti, ^{56}Fe, ^{74}Ge, ^{121}Sb, ^{208}Pb, and ^{238}U. The detailed method was presented in Lan et al. (2017, 2018). Data was handled with ICPMSDataCal using ^{29}Si as the internal standard assuming stoichiometric quartz (Liu et al., 2008; Chen et al., 2011). NIST SRM610 was analyzed as the external standard with element concentrations from Jochum et al. (2011). A natural quartz standard was also used as a secondary standard to ensure accurate results for most trace elements of interest (Audétat et al., 2015). The analysis results show that

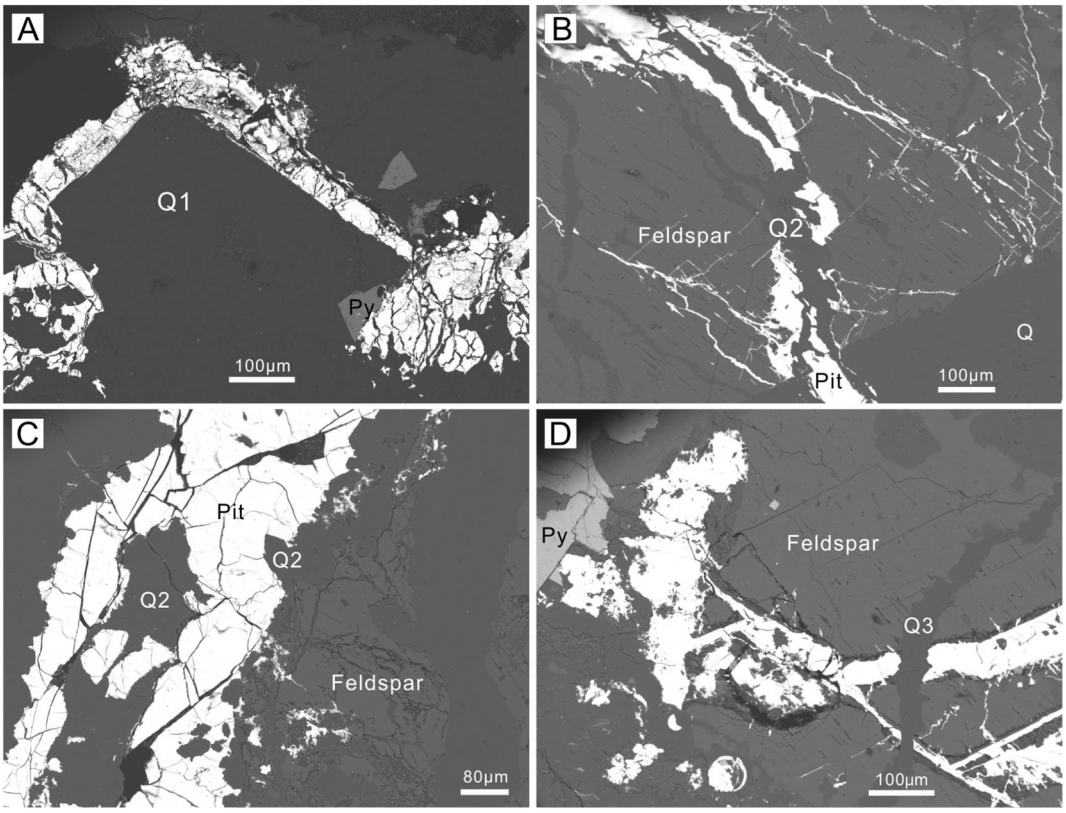

Fig. 4. The back-scattered electron images of the U mineralization in the No. 302 uranium deposit. Q: Quartz; Q1: pre-ore quartz; Q2: *syn*-ore quartz and Q3: post-ore quartz. Pit: Pitchblende; Py: Pyrite.

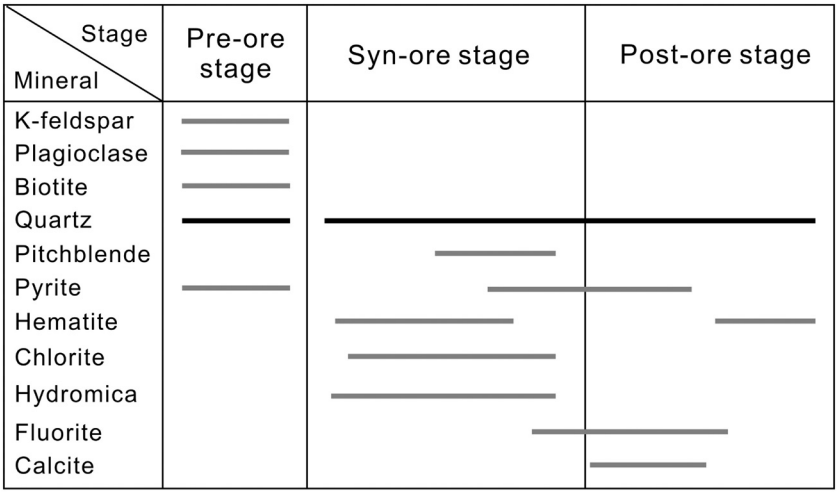

Fig. 5. Simplified paragenesis of major ore and gangue minerals in the No. 302 uranium deposit (modified after Zhang et al., 2017a).

the contents of Ti, Al, Li, Fe and Ge elements in this quartz standard consistently lie within the error range of the preferred values.

4. Results

4.1. CL textures and intensity in quartz

Several basic types of quartz crystals (grains) were defined based on their features under optical microscope and internal fabrics visualized using SEM-CL images. The pre-ore quartz (Q1) usually displays the dark and homogeneous (or slightly mottled) luminescent texture (Fig. 6A, B). Some fragments of quartz with bright luminescence can be also present in Q1 (Fig. 6B). The *syn*-ore quartz (Q2) in quartz-pitchblende (−pyrite) vein shows strong luminescence intensities and is characterized by a well-recognized growth zoning and euhedral and hexagonal quartz crystals (Fig. 6). The most common CL textures in syn-ore quartz include: (i) the rounded or wavy concentric zonation (Q2a in Fig. 6A); (ii) the euhedral growth zones showing oscillatory CL intensity (Q2a in Fig. 6B). The two types of growth zones (Q2a) are commonly characterized by growing from the rim of quartz grain (Q1) towards the crack or pitchblende; (iii) the bright and oscillatory luminescent strip that parallel to the rim of Q1 (Q2a in Fig. 6C). This CL-bright strip is

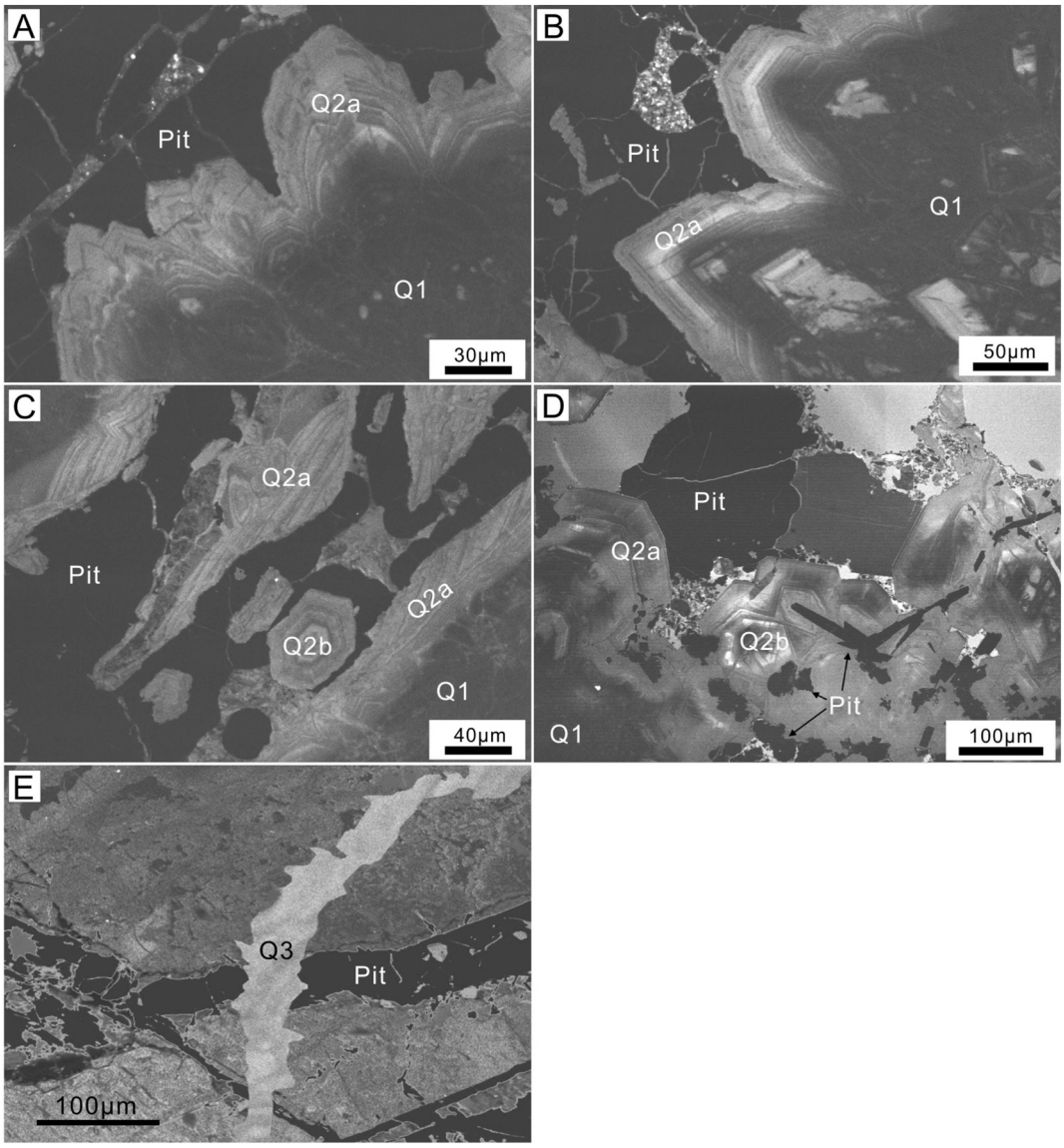

Fig. 6. Typical SEM-CL textures in quartz from No. 302 uranium deposit. A and B: the darker and homogeneous (or slightly mottled) CL textures of Q1 and the CL-bright wavy concentric zonation and the euhedral growth zones of Q2. Some fragments of quartz with bright luminescence were observed inside the Q1, which may result from the incomplete annealing of original CL textures in Q1. C: the bright and oscillatory luminescent strip and the euhedral and hexagonal quartz crystals with bright and concentric oscillatory luminescent textures. D: the Q2 overgrows pitchblende. E: the post-ore quartz (Q3) chiefly cuts the quartz-pitchblende vein and display bright and homogeneous luminescence texture.

generally the contact zone between quartz (Q1) and pitchblende; (iv) the euhedral and hexagonal quartz crystals with bright and concentric oscillatory luminescent texture (Q2b in Fig. 6C, D). The quartz crystals are usually cemented by or closely intergrowth with pitchblende, indicating that they were precipitated directly from the ore-forming fluid. The post-ore quartz (Q3) chiefly cuts the quartz-pitchblende vein and display bright and homogeneous luminescence texture (Fig. 4D, 6E).

4.2. Trace element concentrations in quartz

Electron microprobe analyses can offer a higher spatial resolution than the LA-ICP-MS analytical techniques, although the detection limits are generally too high to detect all trace elements in quartz. A consistent variation of Si and Al concentrations is observed from the core of Q1 to rim on euhedral growth zones (Q2a) (Table 1; Fig. 7). The Q1 have higher Al concentration ranging from 0.15–0.37 wt% (average 0.25 wt %) than the Q2a that have Al concentration varying from 0.06–0.17 wt% (average 0.10 wt%). However, the Si concentration shows inverse variation ranging from 46.06 to 46.90 wt% (average 45.64 wt%) for Q1 and from 45.17 to 46.02 wt% (average 46.49 wt%) for Q2a (Fig. 7). The K and Ca concentrations are generally as low as 0.01–0.04 wt% and 0.02–0.07 wt%, respectively, but roughly correlate positively with Al concentration and negatively with Si content (Fig. 7). Other trace elements are commonly present in concentrations below detection limits of EMPA.

The LA-ICPMS trace elements in quartz from the No. 302 uranium deposit are presented in Table 2. Aluminum is the most abundant trace element in various generations of quartz, with concentrations of 1840 to 4900 ppm for Q1 (average 3367 ppm), 169 to 1816 ppm (average 1001 ppm) for Q2 and 176 to 607 ppm (average 348 ppm) for Q3. Titanium concentration in most spots of Q1 and Q2 is commonly lower than 6.41 ppm and cannot be detected in Q3 except one spot (1.08 ppm). Lithium concentration varies from 1.3 to 493.1 ppm (average 240.3 ppm) in Q1, 2.5 to 295.8 (average 100.6 ppm) in Q2 and 12.5 to 53.7 ppm (average 29.7) in Q3, respectively. K and Na concentrations range from 33.0 to 207.5 ppm and 33.5 to 175.9 ppm in Q1, 20.7 to 135.2 ppm and 17.3 to

Table 1
The representative EMPA analysis (wt%) of quartz from the No. 302 uranium deposit. b.d.l.: below detection limits.

No.	Spots	Si	Al	Ti	K	Ca	Fe	Ge
1	ZK2-1cQ-9	45.53	0.23	b.d.l.	0.04	0.07	0.03	b.d.l.
2	ZK2-1cQ-10	45.50	0.20	b.d.l.	0.02	0.04	b.d.l.	b.d.l.
3	ZK2-1cQ-11	45.67	0.20	b.d.l.	0.02	0.04	0.05	b.d.l.
4	ZK2-1cQ-12	45.53	0.22	b.d.l.	0.02	0.05	b.d.l.	b.d.l.
5	ZK2-1cQ-13	45.76	0.17	b.d.l.	b.d.l.	b.d.l.	0.07	b.d.l.
6	ZK2-1cQ-14	45.90	0.15	b.d.l.	b.d.l.	0.02	b.d.l.	b.d.l.
7	ZK2-1cQ-15	45.88	0.16	b.d.l.	b.d.l.	b.d.l.	b.d.l.	b.d.l.
8	ZK2-1cQ-16	46.02	0.15	b.d.l.	b.d.l.	b.d.l.	b.d.l.	b.d.l.
9	ZK2-1cQ-17	46.55	0.08	b.d.l.	b.d.l.	b.d.l.	b.d.l.	b.d.l.
10	ZK2-1cQ-18	46.62	0.08	b.d.l.	b.d.l.	0.04	b.d.l.	b.d.l.
11	ZK2-1cQ-19	46.54	0.09	b.d.l.	b.d.l.	0.02	b.d.l.	b.d.l.
12	ZK2-1cQ-20	46.57	0.08	b.d.l.	b.d.l.	0.06	b.d.l.	b.d.l.
13	ZK2-1cQ-21	46.36	0.08	b.d.l.	b.d.l.	0.06	0.04	b.d.l.
14	ZK2-1cQ-22	46.53	0.06	b.d.l.	b.d.l.	b.d.l.	b.d.l.	b.d.l.
15	MHK07-2Q-1	45.23	0.35	b.d.l.	0.03	0.04	0.13	b.d.l.
16	MHK07-2Q-2	45.38	0.28	b.d.l.	0.04	0.07	b.d.l.	b.d.l.
17	MHK07-2Q-3	45.31	0.31	b.d.l.	0.04	0.06	b.d.l.	b.d.l.
18	MHK07-2Q-4	45.21	0.33	b.d.l.	0.03	0.04	0.16	b.d.l.
19	MHK07-2Q-5	45.44	0.31	b.d.l.	0.02	0.04	b.d.l.	b.d.l.
20	MHK07-2Q-6	45.17	0.30	b.d.l.	0.04	0.04	b.d.l.	b.d.l.
21	MHK07-2Q-7	45.54	0.37	b.d.l.	b.d.l.	b.d.l.	b.d.l.	b.d.l.
22	MHK07-2Q-8	45.74	0.36	b.d.l.	b.d.l.	b.d.l.	b.d.l.	b.d.l.
23	MHK07-2Q-9	45.66	0.32	b.d.l.	b.d.l.	0.02	b.d.l.	b.d.l.
24	MHK07-2Q-10	45.34	0.31	b.d.l.	0.04	0.04	b.d.l.	b.d.l.
25	MHK07-2Q-11	45.93	0.29	b.d.l.	b.d.l.	0.02	b.d.l.	b.d.l.
26	MHK07-2Q-12	45.89	0.29	b.d.l.	b.d.l.	b.d.l.	b.d.l.	b.d.l.
27	MHK07-2Q-13	45.84	0.32	b.d.l.	0.02	0.02	b.d.l.	b.d.l.
28	MHK07-2Q-14	45.85	0.31	b.d.l.	b.d.l.	b.d.l.	b.d.l.	b.d.l.
29	MHK07-2Q-15	46.69	0.10	b.d.l.	b.d.l.	b.d.l.	b.d.l.	b.d.l.
30	MHK07-2Q-16	46.68	0.15	b.d.l.	b.d.l.	b.d.l.	b.d.l.	b.d.l.
31	MHK07-2Q-17	46.90	0.07	b.d.l.	b.d.l.	b.d.l.	b.d.l.	b.d.l.
32	MHK07-2Q-18	46.70	0.17	b.d.l.	b.d.l.	b.d.l.	b.d.l.	b.d.l.
33	MHK07-2Q-19	46.86	0.17	b.d.l.	b.d.l.	b.d.l.	b.d.l.	b.d.l.
34	MHK07-2Q-20	46.65	0.14	b.d.l.	b.d.l.	b.d.l.	b.d.l.	b.d.l.
35	MHK07-2Q-21	46.51	0.14	b.d.l.	b.d.l.	b.d.l.	b.d.l.	b.d.l.
36	MHK07-2Q-22	46.48	0.07	b.d.l.	b.d.l.	b.d.l.	b.d.l.	b.d.l.
37	MHK07-2Q-23	46.33	0.08	b.d.l.	0.02	b.d.l.	b.d.l.	b.d.l.
38	MHK07-2Q-24	46.48	b.d.l.	b.d.l.	b.d.l.	b.d.l.	b.d.l.	b.d.l.
39	MHK07-2Q-25	46.17	0.11	b.d.l.	b.d.l.	b.d.l.	b.d.l.	b.d.l.
40	MHK07-2Q-26	46.62	0.06	b.d.l.	b.d.l.	b.d.l.	b.d.l.	b.d.l.
41	ZK83Q-6	45.84	0.21	b.d.l.	0.04	0.04	b.d.l.	b.d.l.
42	ZK83Q-7	45.64	0.20	b.d.l.	0.03	0.03	b.d.l.	b.d.l.
43	ZK83Q-8	45.96	0.19	b.d.l.	0.02	0.04	b.d.l.	b.d.l.
44	ZK83Q-9	45.57	0.17	b.d.l.	0.03	b.d.l.	b.d.l.	b.d.l.
45	ZK83Q-10	45.74	0.15	b.d.l.	0.02	0.03	b.d.l.	b.d.l.
46	ZK83Q-11	45.69	0.19	b.d.l.	0.03	0.04	b.d.l.	b.d.l.
47	ZK83Q-12	45.60	0.18	b.d.l.	b.d.l.	0.03	b.d.l.	b.d.l.
48	ZK83Q-13	45.97	0.18	b.d.l.	b.d.l.	0.04	b.d.l.	b.d.l.
49	ZK83Q-14	46.32	0.10	b.d.l.	b.d.l.	b.d.l.	b.d.l.	b.d.l.
50	ZK83Q-15	46.27	0.08	b.d.l.	0.02	b.d.l.	b.d.l.	b.d.l.
51	ZK83Q-16	46.06	0.11	b.d.l.	b.d.l.	b.d.l.	b.d.l.	b.d.l.
52	ZK83Q-17	46.43	0.11	b.d.l.	b.d.l.	0.02	b.d.l.	b.d.l.
53	ZK83Q-18	46.54	0.06	b.d.l.	b.d.l.	0.02	b.d.l.	b.d.l.
54	ZK83Q-19	46.13	0.11	b.d.l.	b.d.l.	b.d.l.	b.d.l.	b.d.l.
55	ZK83Q-20	46.23	0.10	b.d.l.	0.02	b.d.l.	b.d.l.	b.d.l.

161.7 ppm in Q2, and 32.9 to 70.0 ppm and 24.9 to 53.2 ppm in Q3. Most of the spots have Rb concentration of <10 ppm, and the rests are falling in the range of 10 to 20 ppm. Calcium concentration is 37.2 to 311.3 ppm (average 199.9 ppm) in Q1 and 7.1 to 222.9 ppm in Q2 and 5.8 to 59.6 ppm in Q3, respectively. Ge and Sb concentrations are generally lower than 12.88 ppm and 99.9 ppm, respectively, in various quartz generations. Fe concentration in quartz varies largely from 2.6 to 903.2 ppm with the majority of <50 ppm. U and Pb in most Q1 and Q3 are below the detection limits except for two spots in Q1 (240 ppm for Pb; 29 and 18,739 ppm for U). However, U and Pb concentrations in Q2 are 8 to 13,135 ppm and 9 to 299 ppm, respectively.

5. Discussion

5.1. CL textures and environment of formation for quartz

CL textural variations can reflect deposit-scale fluctuations of physiochemical conditions rather than a local fluctuation (Rusk et al., 2008a, 2011). Thus, it can be used to unravel the physico-chemical history of a hydrothermal system (Rusk, 2012). Strongly variable cathodoluminescence intensities are observed in the quartz from No. 302 uranium deposit. The pre-ore quartz (Q1) generally shows dark and homogeneous (or slightly mottled) luminescent texture (Fig. 6), which is similar to characteristics of quartz from orogenic Au deposits and metamorphism with CL textures of homogenous and mottled textures that result from annealing of original CL textures (Seyedolali et al., 1997; Boggs et al., 2002; Monecke et al., 2002; Breiter et al., 2017a). Thus, the CL textures of Q1 are probably generated by the annealing of original CL textures, most likely caused by ore-forming fluid. Some fragments of quartz with bright luminescence were also present inside

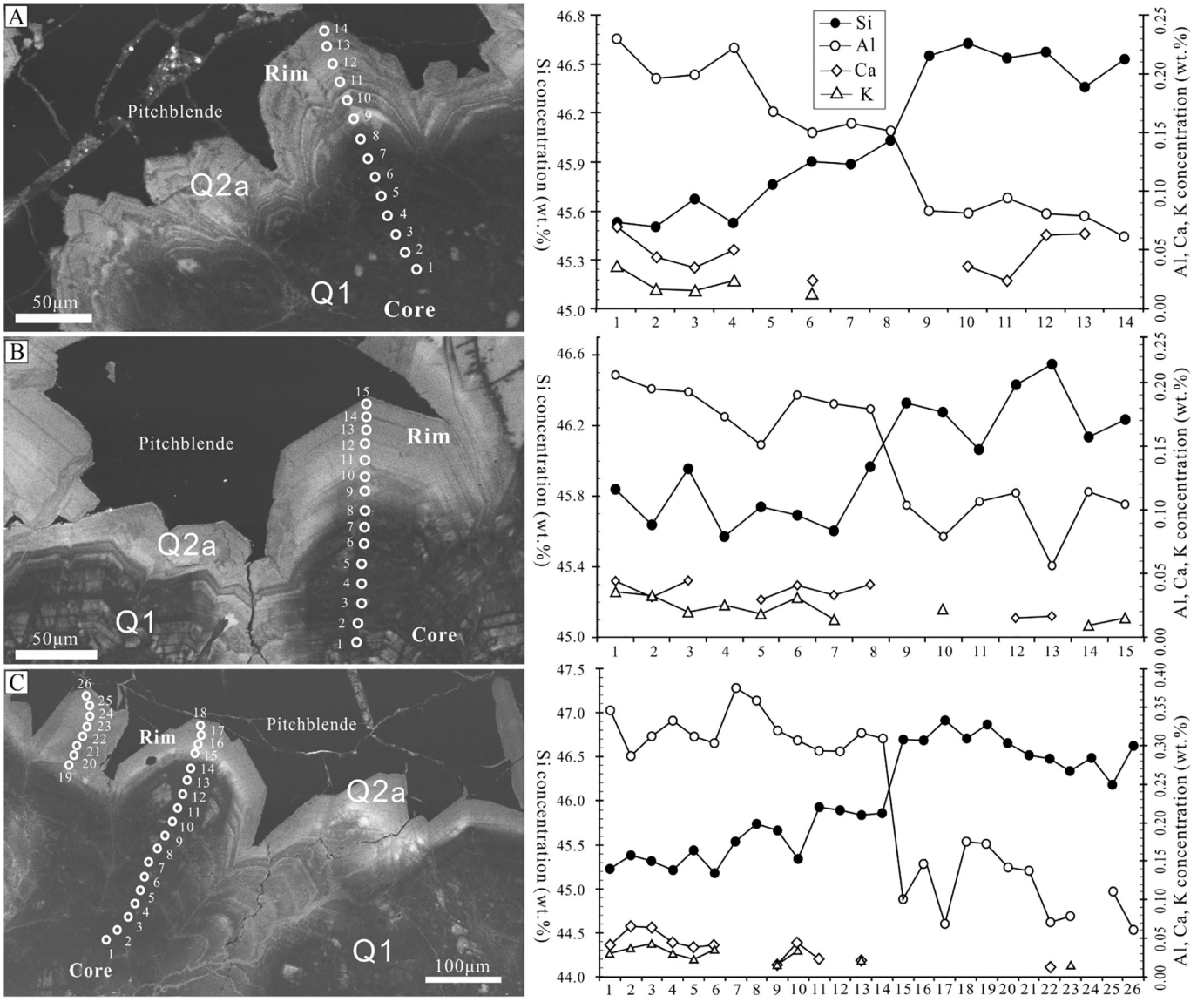

Fig. 7. The CL images of quartz (Left) and corresponding element variation (Right). Trace elements were acquired by electron microprobe. Aluminum concentrations negatively correlate very closely with CL intensity. The hollow symbols refer to the right axis.

the Q1 (Fig. 6B), which may result from the incomplete annealing of original CL textures in Q1.

The Q2 is usually present as euhedral growth zones (Q2a) and euhedral and hexagonal quartz crystals (Q2b), which show bright and oscillatory luminescent texture. The Q2a generally forms on the rim of Q1 suggesting it was formed after Q1. The pitchblende can overgrow around Q2 (Fig. 6A, B), or occur as cements for quartz grains (Fig. 6C) and sometimes Q2 overgrows pitchblende (Fig. 6D), indicating this generation of quartz simultaneously precipitated with pitchblende from ore-forming fluid. Under cross-polarized light, the Q2 in quartz-pitchblende vein and quartz-pitchblende-pyrite vein display micro-crystalline and comb features that was widely considered as the typical characteristics of *syn*-ore quartz in this deposit (Fig. 3D, F; Feng et al., 2009; Bonnetti et al., 2018).

The syn-ore quartz (Q2) usually displays oscillatory growth fabrics that are commonly observed in hydrothermal vein quartz (Rusk, 2012), probably indicating a hydrothermal origin. Euhedral growth zones are predominantly present in epithermal and other low temperature quartz (Rusk et al., 2008a; Lehmann et al., 2009; Rusk, 2012), suggesting that the syn-ore Q2 in this deposit may have precipitated from low-temperature fluids, which is also supported by fluid-inclusion data (Zhang, 2008; Guo et al., 2010; Zhang et al., 2017a).

The post-ore quartz (Q3) chiefly cuts the quartz-pitchblende vein and display bright and homogeneous CL texture, which reflect that the Q3 quartz precipitated under stable physico-chemical conditions (Götte et al., 2011).

5.2. *Trace elements in quartz and their relationship with cathodoluminescence*

Quartz generally has a simple chemical composition, and just a few of elements can incorporate into quartz crystal (Götze, 2009; Müller et al., 2012). The LA-ICPMS depth profiles show that elements including Al, Li, K, Na and Ca, have relatively smooth signals that are consist of a series of small and comparative peaks (Fig. 8), suggesting that these elements may mainly occur as solid solution within the crystal lattice or at least as invisible nanoparticles in quartz (Genna and Gaboury, 2015; Dehnavi et al., 2018). The high variability of concentrations and irregular depth profiles for Sb, Rb, Ti, Ge and Fe imply that they may be primarily incorporated into quartz as both solid solution and micro-inclusion, and U may be primarily present as mineral inclusion of pitchblende in syn-ore quartz (Cook et al., 2009; Ciobanu et al., 2013).

Table 2
The LA-ICPMS analysis of trace element concentrations (ppm) for each generation of quartz from the No. 302 uranium deposit.

No.	Comment	Al	Ti	Li	K	Na	Rb	Ca	Ge	Sb	Fe	Pb	U
Quartz 1													
1	ZK2-1cQ-03	4900	–	493.1	119.1	158.7	9.58	311.3	3.92	–	9.9	–	–
2	ZK2-1cQ-08	4166	1.76	180.5	132.1	162.7	5.72	301.1	1.34	18.0	24.6	–	–
3	ZK2-1cQ-11	3357	6.41	190.5	139.7	95.8	8.92	257.6	7.79	12.2	13.8	–	–
4	ZK2-1cQ-12	1840	3.73	155.3	98.7	33.5	7.29	169.9	6.05	3.7	36.9	–	–
5	MHK07-2Q-1	4744	–	405.8	170.2	74.3	14.52	267.2	3.82	5.0	16.2	–	–
6	MHK07-2Q-7	4647	–	369.3	33.0	175.9	10.28	80.1	4.15	89.1	4.1	–	–
7	MHK07-2Q-4	3072	1.26	302.0	119.7	79.5	5.95	187.2	2.99	33.3	7.7	–	–
8	MHK07-3Q-3	3742	1.60	391.8	78.5	117.0	5.76	194.1	9.82	59.4	5.9	–	–
9	MHK07-3Q-4	2975	–	1.3	207.5	129.0	5.52	37.2	5.61	–	10.1	–	–
10	MHK07-3Q-8	2528	–	4.0	174.2	98.6	1.02	179.2	7.92	6.2	2.6	–	–
11	ZK83Q-1	4285	–	396.7	104.4	153.3	18.63	272.0	4.53	–	4.4	–	–
12	ZK83Q-2	1956	1.28	193.0	114.8	87.1	3.54	121.4	4.55	62.2	7.4	240	18,739
13	ZK83Q-3	2229	3.87	208.0	136.9	75.0	15.41	237.1	–	38.1	477.7	–	–
14	ZK83Q-5	3318	1.37	71.5	109.7	161.5	5.71	228.2	5.42	14.6	45.5	–	29
15	ZK83Q-8	2751	1.31	241.2	59.5	107.3	3.58	154.1	7.01	1.6	55.0	–	–
Quartz 2													
16	ZK2-1cQ-01	1056	–	95.6	91.3	73.4	0.98	221.4	12.88	45.2	4.2	–	–
17	ZK2-1cQ-02	744	2.88	72.3	45.6	103.1	5.17	57.1	11.80	85.2	3.0	299	13,136
18	ZK2-1cQ-04	733	1.43	56.3	53.9	122.7	5.67	135.7	–	47.1	82.4	129	2115
19	ZK2-1cQ-05	1178	3.23	137.3	49.8	123.3	10.90	135.7	–	32.1	534.4	–	152
20	ZK2-1cQ-06	1326	1.47	176.2	33.2	134.9	3.30	85.7	8.43	7.1	328.8	–	8
21	ZK2-1cQ-07	696	–	77.4	44.1	128.6	5.30	128.6	–	–	121.7	–	–
22	ZK2-1cQ-09	537	1.48	43.9	87.7	42.0	4.94	71.4	6.88	87.2	21.6	–	–
23	ZK2-1cQ-10	776	4.16	69.7	51.8	75.9	3.48	35.7	–	51.2	63.8	–	–
24	MHK07-2Q-2	1493	2.60	2.5	57.2	156.6	6.02	222.9	5.03	35.2	5.6	–	–
25	MHK07-2Q-3	339	–	35.2	49.8	74.1	15.05	7.1	7.10	12.5	8.5	–	–
26	MHK07-2Q-5	1099	–	106.9	20.7	137.6	12.43	92.9	5.67	–	38.6	–	–
27	MHK07-2Q-6	601	–	47.5	76.4	91.6	10.19	7.1	3.90	16.8	22.7	–	–
28	MHK07-3Q-1	169	–	37.9	37.3	48.9	9.60	35.7	–	48.3	903.2	–	85
29	MHK07-3Q-2	1763	2.69	143.7	135.2	77.1	3.97	189.1	7.63	68.2	10.2	9	–
30	MHK07-3Q-5	945	–	98.2	70.5	96.4	4.33	142.9	11.53	99.9	3.7	14	–
31	MHK07-3Q-6	1289	1.06	139.7	37.3	161.7	7.55	150.0	–	12.6	3.2	–	–
32	MHK07-3Q-7	519	1.27	47.4	76.6	50.6	2.48	114.3	9.81	71.5	224.1	221	7541
33	ZK83Q-4	1660	–	168.7	132.5	20.7	7.24	178.6	6.25	97.2	147.2	–	–
34	ZK83Q-6	1279	5.87	159.7	41.5	48.9	6.26	176.4	3.95	–	23.6	290	8631
35	ZK83Q-7	1816	2.66	295.7	103.7	17.3	7.73	191.4	5.05	59.3	5.5	–	–
Quartz 3													
36	ZK83-5Q-1	319	–	29.0	57.2	39.0	4.39	31.1	–	–	–	–	–
37	ZK83-5Q-2	176	–	12.5	34.5	24.9	–	5.8	–	–	–	–	–
38	ZK83-5Q-3	607	–	53.7	70.0	49.1	5.24	59.6	3.97	–	5.3	–	–
39	ZK83-5Q-4	221	1.08	15.3	38.1	25.4	–	8.2	–	–	–	–	–
40	ZK83-5Q-5	294	–	24.5	33.5	49.8	–	15.0	–	3.8	–	–	–
41	ZK83-5Q-6	520	–	49.7	68.0	43.3	2.87	37.6	–	–	–	–	–
42	ZK83-5Q-7	260	–	19.5	32.9	53.1	–	10.2	2.75	–	3.0	–	–
43	ZK83-5Q-8	383	–	33.3	52.5	35.2	–	18.7	–	–	–	–	–

As Sb does not correlate with other trace elements, thus, the Sb incorporated into quartz as inclusion or in other form that requires to be further studied. Large variations of Fe concentrations in Q1 and Q2 indicate some spots may be affected by mineral micro-inclusions beneath surface (e.g. pyrite or hematite), as suggested by previous studies that showed that Fe can be incorporated into quartz both as substitutional ion for Si and bound on mineral micro-inclusions (Rusk, 2012), which is also supported by the LA-ICPMS depth profiles that show Fe may primarily incorporate into quartz in the form of both solid solution and micro-inclusion (Fig. 8). The U concentration in most of the spots in Q1 and Q2 is commonly below detection limit, except a few spots up to a few 1000 ppm, indicating that U primarily present as micro-inclusion (e.g. pitchblende) in quartz, which is consistent with the abnormal signal of U in depth profiles (Fig. 8). The Ge, Sb, Fe, Pb and U in most of the analyzed spots in Q3 are below detection limits, which suggest that the Q3 has significantly lower contents of trace elements than Q1 and Q2, which is in accordance with the stable conditions that Q3 precipitated (Götte et al., 2011).

Of the trace elements that are commonly identified in various generations of quartz, aluminum is typically the most abundant. Al concentration in quartz from No. 302 uranium deposit shows obviously decreasing from Q1 to Q2 and Q3 (Table 1). The high Al concentration of pre-ore quartz (Q1) likely reflected the low pH value of fluid from which Q1 precipitated (Rusk et al., 2008a). The Al content in syn-ore quartz (Q2) ranges from 169 to 1816 ppm, which is similar to that of low-temperature hydrothermal quartz (Rusk et al., 2008a), probably indicative of a hydrothermal origin. The post-ore quartz (Q3) has significantly lower Al concentration (176 to 607 ppm), which is consistent with the quartz precipitated under stable thermodynamic conditions, which has moderate to low trace element concentrations (Götte et al., 2011).

The positive linear correlations between aluminum and (K + Na) and Li are observed in various generations of quartz (Fig. 9), suggesting that K, Na and Li are likely incorporated in quartz as charge-compensated cations in the substitution of $Si^{4+} \leftrightarrow Al^{3+} + (K^{+}, Na^{+}, Li^{+})$ (Rusk et al., 2008a). This excellent correlation also implied the trace element in the analyzed spots was hardly affected by the inclusions in which the K and Na are generally enriched. This is also supported by the smooth signals of these elements in LA-ICPMS depth profiles (Fig. 8). A positive correlation between Ca and Al in various generations of quartz may reflect the incorporation of Ca, to charge balance Al, which substitutes for Si (Fig. 7c; Rusk et al., 2008a). Additionally, a weak negative correlation between Ge and Al suggest that Ge may substitute Si independently due to the similar charge (Fig. 7d).

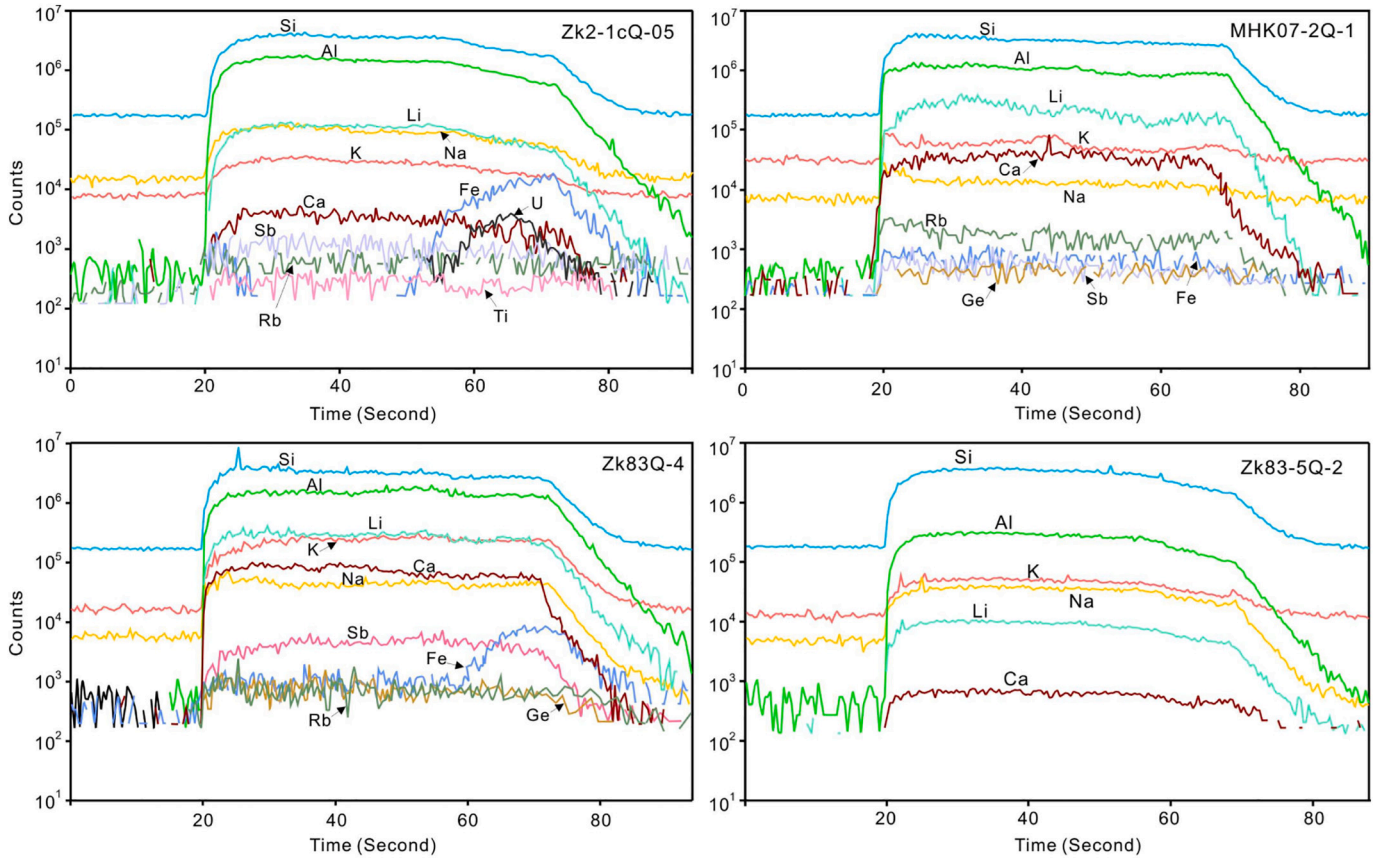

Fig. 8. Representative LA-ICPMS depth profile for major trace elements in quartz from the No. 302 uranium deposit.

Previous studies have shown that CL intensity generally correlates positively with titanium concentrations, and thus the Ti usually act as a CL activator in quartz formed at >400 °C (Rusk et al., 2008a, 2011). Ti concentrations in Q1 are generally lower than 6.41 ppm, which are lower than those of high-temperature (>400 °C) quartz that have Ti concentration > 10 ppm (Rusk et al., 2008a). Combining with the annealed dark and homogeneous (or slightly mottled) luminescent texture, the Q1 may have experienced the alteration by ore-forming fluids, which led to the annealing of its original CL textures and the decrease of Ti content.

Titanium concentrations in Q2 are generally lower than 6 ppm (Table 2), which is similar to those in low-temperature quartz, implying that the temperature of quartz-precipitating hydrothermal fluids is <350 °C (Rusk et al., 2008a). Thus, it can be believed that the ore-forming temperature of quartz-pitchblende vein in the No. 302 uranium deposit could be below 350 °C, which is consistent with the results from fluid inclusion studies (Zhang, 2008; Guo et al., 2010; Zhang et al., 2017a). The extremely low Ti concentration in Q3 (generally below detection limits in most analyzed spots) is a typical characteristic of low-temperature quartz (Rusk et al., 2008a).

Though there is no consistent correlation between CL intensity and trace element abundance that applies to all quartz, the CL intensity variations generally coincide with measurable trace element variations (Rusk, 2012). Although Ti, Al and associated monovalent cations are thought to be common CL activators, other cations such as Fe, Ge, P, Sb, K, and Li are also considered to act as CL activators or quenchers in quartz (Frelinger et al., 2015), but no systematic correlations are so far reported. A negative correlation between CL intensity and Al concentration was observed in quartz from No. 302 uranium deposit. For example, the Al concentration shows a sharp decrease from Q1 to Q2; however, the CL intensity shows an inverse trend from dark and homogeneous (or slightly mottled) luminescence texture to bright and oscillatory luminescent texture (Figs. 6, 7), and the Q3 has lowest Al concentration but displays most bright CL intensity. A similar case was reported by Rusk et al. (2008b) that Al negatively correlated with luminescence intensities in quartz from the Butte porphyry Cu deposit. Therefore, the Al and Ti (below detection) are obviously not the CL activators in this deposit, other elements mentioned above probably play the role. For example, variations in CL intensity in natural quartz have been reported to be related to Ge (Götze et al., 2004) or the monovalent cations Li, Na, and K (Demars et al., 1996; Landtwing and Pettke, 2005; Rusk et al., 2006). Thus, the relationships between quartz CL intensity and trace element concentrations require to be further studied.

5.3. Implications for precipitation mechanism of uranium deposits

In the No. 302 uranium deposit, the *syn*-ore quartz (Q2) have remarkably large variation of Al concentration ranging from 169 to 1816 ppm (Tables 1, 2), and other trace elements (such as Li, K, Na, Ca, Sb etc.) also show large variation range (Fig. 10). Earlier studies have shown that drastic changes of trace element concentrations in quartz on a micron scale were interpreted to be caused by the variability in fluid composition and less affected by changes in temperature or growth rate (Perny et al., 1992; Landtwing and Pettke, 2005; Rusk et al., 2008a; Jourdan et al., 2009). Thus, the variation of Al concentrations in syn-ore quartz at the No. 302 uranium deposit is likely reflecting the change of dissolved Al concentrations in ore-forming fluid, which is significantly controlled by pH of the fluid (Perny et al., 1992; Rusk et al., 2008a).

In the No. 302 uranium deposit, the previous studies have shown that the U extracted from the host granites was transported in acid ore-forming fluids in the forms of $UO_2(CO_3)_2^{2-}$ and/or $UO_2(CO_3)_3^{4-}$ (Jin and Hu, 1987; Li, 1989; Deng et al., 2003; Hu et al., 2009; Luo, 2015). The fluid inclusion study suggests that the ore-forming fluids underwent

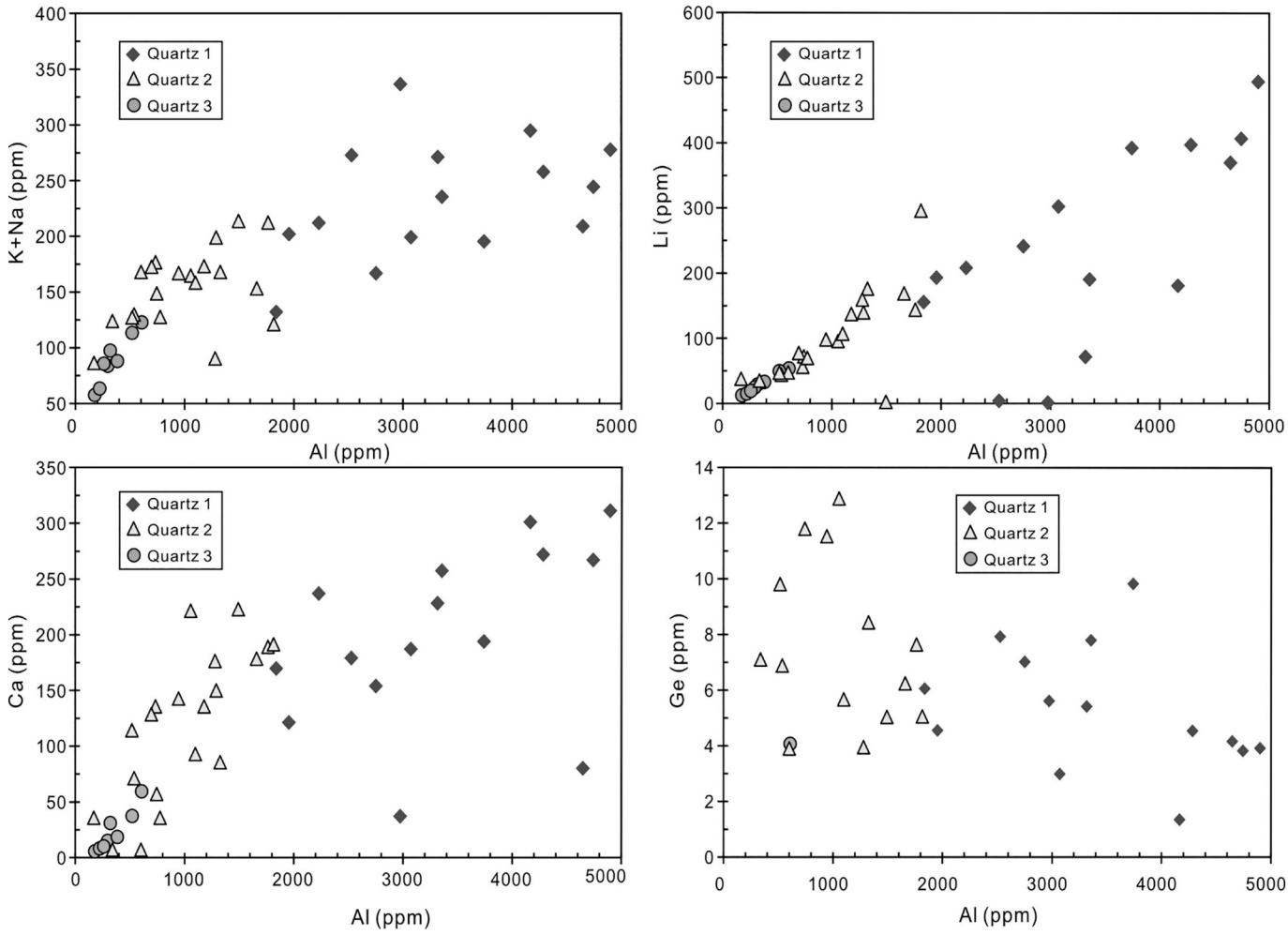

Fig. 9. Correlation between Al and other trace elements in quartz from the No. 302 uranium deposit.

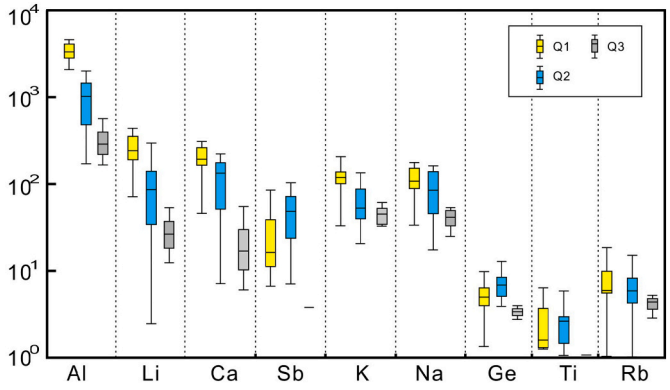

Fig. 10. Box diagram of trace element concentrations for the various generations of quartz from the No. 302 uranium deposits in southern China.

CO_2 effervescence or phase separation at about 250 °C under a pressure of 1000–1100 bar (Zhang et al., 2017a), which could result in the decomposition of uranyl carbonate complexes ($UO_2(CO_3)^{2-}$) and the rise of pH value of ore-forming fluid, and the decrease of Al solubility in ore-forming fluids and thus lead to the large variation of Al concentrations in syn-ore quartz. The variation of pH value would lead to a change of the mineral assemblage from quartz-kaolinite to quartz-illite (Lehmann et al., 2011). Such a transition could have taken place because of the presence of abundant hydromica (illite) and little kaolinite in this deposit (Huang et al., 2015; Zhang et al., 2017a). Meanwhile, previous studies also show that the pH value of ore-forming fluid had a significant increase during uranium mineralization (Li, 1989). Furthermore, Rusk et al. (2008a) proposed that the neutralization of an acidic hydrothermal fluid is a common mechanism of metal sulfide precipitation, and Al concentrations in quartz can serve as a proxy for the processes leading to ore precipitation.

6. Conclusions

The SEM-CL texture and trace elements composition of quartz from 302 uranium deposit, South China suggest that the dark and homogeneous (or slightly mottled) luminescent texture of pre-ore quartz (Q1) probably results from annealing of original CL textures caused by ore-forming fluid, and the syn-ore quartz (Q2) has a typical characteristic of low-temperature quartz. The Al and Ti are obviously not the major CL activators in quartz in this deposit. The ore-forming fluid in the No. 302 uranium deposit could be a low-temperature fluid from which the quartz-pitchblende vein precipitated. The large variation range of trace elements in syn-ore quartz was likely caused by the change of pH value of ore-forming fluid, probably resulting from the CO_2 effervescence or phase separation occurred from ore-forming fluid, which would have led to uranyl carbonate complexes ($UO_2(CO_3)^{2-}$) decomposing and and thus finally caused the precipitation of pitchblende. The luminescence texture and low concentration of trace elements of post-ore quartz (Q3) reflect its precipitation under stable physical and chemical conditions.

CRediT authorship contribution statement

Qing Lan: Conceptualization, Methodology, Investigation, Software, Data curation, Writing – original draft. **Jinrong Lin:** Investigation, Resources, Funding acquisition, Writing – review & editing. **Shanling Fu:** Writing – review & editing, Funding acquisition. **Jincheng Luo:** Investigation, Writing – review & editing.

Declaration of competing interest

The authors declare that they have no known competing financial interests or personal relationships that could have appeared to influence the work reported in this paper.

Acknowledgement

This work was financially supported by jointly the projects of the National Key R&D Program of China (2017YFC0602601), National Natural Science Foundation of China (41702101, 42072098), West light Foundation of the Chinese Academy of Science, and the Strategic Priority Research Program (B) of Chinese Academy of Sciences (Grant No. XDB18000000). The authors are indebted to the colleagues from the Research Institute No. 290, Bureau of Geology of the Chinese National Nuclear Corporation in Shaoguan, Guangdong, for their field support and the access to the mine sites. We also thank Dr. Yanwen Tang for the assistance with LA-ICPMS analysis and Dr. Xiang Li for the acquisition of EPMA data.

References

Audétat, A., Garbe-Schönberg, D., Kronz, A., Pettke, T., Lowers, H.A., 2015. Characterisation of a Natural Quartz Crystal as a Reference Material for Microanalytical Determination of Ti, Al, Li, Fe, Mn, Ga and Ge. Geostandards & Geoanalytical Research 39, 171–184.

Baele, J.M., Decrée, S., Rusk, B., 2019. Cathodoluminescence Applied to Ore Geology and Exploration, In: Decrée, S., Robb, L. (Eds.), Ore Deposits: Origin, Exploration, and Exploitation. American Geophysical Union, 131–161.

Boggs, S., Kwon, Y.I., Goles, G.G., Rusk, B.G., Krinsley, D., Seyedolali, A., 2002. Is Quartz Cathodoluminescence Color a Reliable Provenance Tool? A Quantitative Examination. J. Sediment. Res. 72, 408–415.

Bonnetti, C., Liu, X., Mercadier, J., Cuney, M., Deloule, E., Villeneuve, J., Liu, W., 2018. The genesis of granite-related hydrothermal uranium deposits in the Xiazhuang and Zhuguang ore fields, North Guangdong Province, SE China: Insights from mineralogical, trace elements and U-Pb isotopes signatures of the U mineralisation. Ore Geol. Rev. 92, 588–612.

Breiter, K., Ďurišová, J., Dosbaba, M., 2017a. Quartz chemistry – a step to understanding magmatic-hydrothermal processes in ore-bearing granites: Cínovec/Zinnwald Sn-W-Li deposit, Central Europe. Ore Geol. Rev. 90, 25–35.

Breiter, K., Korbelová, Z., Chládek, Š., Uher, P., Knesl, I., Rambousek, P., Honig, S., Šešulka, V., 2017b. Diversity of Ti–Sn–W–Nb–Ta oxide minerals in the classic granite-related magmatic–hydrothermal Cínovec/Zinnwald Sn–W–Li deposit (Czech Republic). Eur. J. Mineral. 29, 727–738.

Charvet, J., 2013. The Neoproterozoic–Early Paleozoic tectonic evolution of the South China Block: an overview. J. Asian Earth Sci. 74, 198–209.

Chen, L., Liu, Y., Hu, Z., Gao, S., Zong, K., Chen, H., 2011. Accurate determinations of fifty-four major and trace elements in carbonate by LA–ICP-MS using normalization strategy of bulk components as 100%. Chem. Geol. 284, 283–295.

Ciobanu, C.L., Cook, N.J., Kelson, C.R., Guerin, R., Kalleske, N., Danyushevsky, L., 2013. Trace element heterogeneity in molybdenite finger prints stage of mineralization. Chem. Geol. 347, 175–189.

Cook, N.J., Ciobanu, C.L., Pring, A., Skinner, W., Shimizu, M., Danyushevsky, L., Saini-Eidukat, B., Melcher, F., 2009. Trace and minor elements in sphalerite: a LA-ICPMS study. Geochemica et Cosmochimica Acta 73, 4761–4791.

Crookes, W., 1879. Contributions to molecular physics in high vacua. Magnetic deflection of molecular trajectory. - Laws of magnetic rotation in high and low vacua. - Phosphorogenic properties of molecular discharge. Philosophical Transactions of the Royal Society of London 170, 641–662.

Dahlkamp, F.J., 2009. Uranium Deposits of the World. Springer Ed, Asia, p. 493.

Dehnavi, A.S., McFarlane, C.R.M., Lentz, D.R., Walker, J.A., 2018. Assessment of pyrite composition by LA-ICP-MS techniques from massive sulfide deposits of the Bathurst Mining Camp, Canada: from textural and chemical evolution to its application as a vectoring tool for the exploration of VMS deposits. Ore Geol. Rev. 92, 656–671.

Demars, C., Pagel, M., Deloule, E., Blanc, P., 1996. Cathodoluminescence of quartz from sandstones: interpretation of the UV range by determination of trace element distributions and fluid-inclusion P-T-X properties in authigenic quartz. Am. Mineral. 81, 891–901.

Deng, P., Shen, W.Z., Ling, H.F., Ye, H.M., Wang, X.C., Pu, F., Tan, Z.Z., 2003. Uranium mineralization related to mantle fluid: a case study of the Xianshi deposit in the Xiazhuang uranium orefield. Geochimica 32, 520–528 (in Chinese with English abstract).

Deng, P., Ren, J.S., Ling, H.F., Shen, W.Z., Sun, L.Q., Zhu, B., Tan, Z.Z., 2011. Yanshanian granite batholiths of southern Zhuguang Mountian: SHRIMP zircon U-Pb dating and tectonic implications. Geological Review 57, 881–888 (in Chinese with English abstract).

Deng, P., Ren, J.S., Ling, H.F., Shen, W.Z., Sun, L.Q., 2012. SHRIMP zircon U-Pb ages and tectonic implications for Indosinian granitoids of southern Zhuguangshan granitic composite, South China. Chin. Sci. Bull. 57, 1542–1552.

Feng, H.S., Yin, Z.P., Xu, W.X., Huang, G.L., 2009. Mineralgenetic Characterisitc and Prospecting potential of the deeping of Mianhuakeng uranium deposit in Southern Zhuguang Granite Batholith. Journal of East China Institute of technolohy 32, 101–107 (in Chinese with English abstract).

Frelinger, S.N., Ledvina, M.D., Kyle, J.R., Zhao, D., 2015. Scanning electron microscopy cathodoluminescence of quartz: Principles, techniques and applications in ore geology. Ore Geol. Rev. 65, 840–852.

Fu, S.L., Lan, Q., Yan, J., 2020. Trace element chemistry of hydrothermal quartz and its genetic significance: a case study from the Xikuangshan and Woxi giant Sb deposits in southern China. Ore Geol. Rev. 126, 103732.

Gao, P., Zhao, Z.F., Zheng, Y.F., 2014. Petrogenesis of Triassic granites from the Nanling Range in South China: implications for geochemical diversity in granites. Lithos 210-211, 40–56.

Genna, D., Gaboury, D., 2015. Deciphering the hydrothermal evolution of a VMS system by LA-ICP-MS using trace elements in pyrite: an example from the Bracemac-McLeod Deposits, Abitibi, Canada, and implications for exploration. Econ. Geol. 110, 2087–2108.

Gilder, S.A., Gill, J., Coe, R.S., Zhao, X., Liu, Z., Wang, G., Yuan, K., Liu, W., Kuang, G., Wu, H., 1996. Isotopic and paleomagnetic constraints on the Mesozoic tectonic evolution of south China. J. Geophys. Res. 101, 16137–16154.

Götte, T., Pettke, T., Ramseyer, K., Koch-Müller, M., Mullis, J., 2011. Cathodoluminescence properties and trace element signature of hydrothermal quartz: a fingerprint of growth dynamics. Am. Mineral. 96, 802–813.

Götze, J., 2000. Cathodoluminescence microscopy and spectroscopy in applied mineralogy. Freib. Forsch. 485, 1–128.

Götze, J., 2009. Chemistry, textures and physical properties of quartz – geological interpretation and technical application. Mineralogical Magazine 645–671.

Götze, J., Plötze, M., Habermann, D., 2001. Origin, spectral characteristics and practical applications of the cathodoluminescence (CL) of quartz – a review. Mineral. Petrol. 71, 225–250.

Götze, J., Plötze, M., Graupner, T., Hallbauer, D.K., Bray, C.J., 2004. Trace element incorporation into quartz: a combined study by ICP-MS, electron spin resonance, cathodoluminescence, capillary ion analysis, and gas chromatography 1 1Associate editor: U. W. Reimold. Geochimica et Cosmochimica Acta 68, 3741–3759.

Guo, G.L., Liu, X.D., Pan, J.Y., Liu, C.D., Yan, Z.B., Chen, Y.P., 2010. Study of fluid inclusion from uranium deposit No.302 in north Guangdong. Uranium Geology 26, 350–354 (in Chinese with English abstract).

Hu, R.Z., Zhou, M.F., 2012. Multiple Mesozoic mineralization events in South China-an introduction to the thematic issue. Mineral. Deposita 47, 579–588.

Hu, R.Z., Burnard, P.G., Bi, X.W., Zhou, M.F., Peng, J.T., Su, W.C., Zhao, J.H., 2009. Mantle-derived gaseous components in ore-forming fluids of the Xiangshan uranium deposit, Jiangxi province, China: evidence from He, Ar and C isotopes. Chem. Geol. 266, 86–95.

Hu, R.Z., Chen, W.T., Xu, D.-R., Zhou, M.F., 2017. Reviews and new metallogenic models of mineral deposits in South China: an introduction. Journal of Asian Earth Sciences 137 (Supplement C), 1-8.

Huang, R., Audétat, A., 2012. The titanium-in-quartz (TitaniQ) thermobarometer: a critical examination and re-calibration. Geochim. Cosmochim. Acta 84, 75–89.

Huang, G.L., Cao, H.J., Ling, H.F., Shen, W.Z., Wang, X.D., Fu, S.C., 2012. Zircon SHRIMP U-Pb age, geochemistry and genesis of the Youdong granite in Northern Guangdong. Acta Geol. Sin. 86, 577–586.

Huang, G.L., Cao, H.J., Xu, W.X., Shen, W.Z., 2015. Vertical zoning model and prospecting potential in depth of Mianhuakeng uranium deposit in Zhuguang. Uranium Geology 31, 355–362 (in Chinese with English abstract).

Jin, J.F., Hu, R.Z., 1987. Transportation and deposition of uranium in the hydrothermal ore-forming fluids as exemplified by uranium deposit No. 302. Geochimica 4, 320–329 (in Chinese with English abstract).

Jochum, K.P., Weis, U., Stoll, B., Kuzmin, D., Yang, Q., Raczek, I., Jacob, D.E., Stracke, A., Birbaum, K., Frick, D.A., Günther, D., Enzweiler, J., 2011. Determination of reference values for NIST SRM 610–617 glasses following ISO guidelines. Geostand. Geoanal. Res. 35, 397–429.

Jourdan, A.L., Venneman, T.W., Mullis, J., Ramseyer, K., Spiers, C.J., 2009. Evidence of growth and sector zoning in hydrothermal quartz from Alpine veins. Eur. J. Mineral. 21, 219–231.

Lan, T.G., Hu, R.Z., Fan, H.R., Bi, X.W., Tang, Y.W., Zhou, L., Mao, W., Chen, Y.H., 2017. In-situ analysis of major and trace elements in fluid inclusion and quartz: LA-ICP-MS method and applications to ore deposits. Acta Petrol. Sin. 33, 3239–3262 (in Chinese with English abstract).

Lan, T.G., Hu, R.Z., Bi, X.W., Mao, G.J., Wen, B.J., Liu, L., Chen, Y.H., 2018. Metasomatized asthenospheric mantle contributing to the generation of Cu-Mo deposits within an intracontinental setting: a case study of the ~128Ma Wangjiazhuang Cu-Mo deposit, eastern North China Craton. J. Asian Earth Sci. 160, 460–489.

Landtwing, M.R., Pettke, T., 2005. Relationships between SEM-cathodoluminescence response and trace-element composition of hydrothermal vein quartz. Am. Mineral. 90, 122–131.
Landtwing, M.R., Pettke, T., Halter, W.E., Heinrich, C.A., Redmond, P.B., Einaudi, M.T., Kunze, K., 2005. Copper deposition during quartz dissolution by cooling magmatic–hydrothermal fluids: the Bingham porphyry. Earth Planet. Sci. Lett. 235, 229–243.
Legros, H., Marignac, C., Mercadier, J., Cuney, M., Richard, A., Wang, R.C., Charles, N., Lespinasse, M.-Y., 2016. Detailed paragenesis and Li-mica compositions as recorders of the magmatic-hydrothermal evolution of the Maoping W-Sn deposit (Jiangxi, China). Lithos 264, 108–124.
Lehmann, K., Berger, A., Götte, T., Ramseyer, K., Wiedenbeck, M., 2009. Growth related zonations in authigenic and hydrothermal quartz characterized by SIMS-, EPMA-, SEM-CL- and SEM-CC-imaging. Mineral. Mag. 73, 633–643.
Lehmann, K., Pettke, T., Ramseyer, K., 2011. Significance of trace elements in syntaxial quartz cement, Haushi Group sandstones, Sultanate of Oman. Chem. Geol. 280, 47–57.
Li, T.G., 1989. Geological features of deposits No. 201 and No. 361 and analyses of formation conditions of uranium-rich ore deposits. Uranium Geology 5, 66–71 (in Chinese with English abstract).
Li, X.H., Li, W.X., Wang, X.C., Li, Q.L., Liu, Y., Tang, G.Q., Gao, Y.Y., Wu, F.Y., 2010. SIMS U–Pb zircon geochronology of porphyry Cu–Au–(Mo) deposits in the Yangtze River Metallogenic Belt, eastern China: Magmatic response to early Cretaceous lithospheric extension. Lithos 119, 427–438.
Liu, Y., Hu, Z., Gao, S., Günther, D., Xu, J., Gao, C., Chen, H., 2008. In situ analysis of major and trace elements of anhydrous minerals by LA-ICP-MS without applying an internal standard. Chem. Geol. 257, 34–43.
Luo, J.C., 2015. Genesis of Granite-hosted Uranium Deposits in the Northern Guangdong. Constraints from mineralogy, uranium mineral U-Pb geochronology and geochemistry. Unpublished D.Sc. thesis, the University of Chinese Academy of Sciences, China, pp. 1–179 (in Chinese with English abstract).
Mao, J., Cheng, Y., Chen, M., Franco, P., 2013. Major types and time–space distribution of Mesozoic ore deposits in South China and their geodynamic settings. Mineral. Deposita 48, 267–294.
Mao, J.W., Ouyang, H.G., Song, S.W., Santosh, M., Yuan, S.D., Zhou, Z.H., Zheng, W., Liu, H., Liu, P., Cheng, Y.B., Chen, M.H., 2019. Geology and metallogeny of tungsten and tin deposits in China: Society of Economic Geologists. Special Publication 22, 411–482.
Monecke, T., Kempe, U., Götze, J., 2002. Genetic significance of the trace element content in metamorphic and hydrothermal quartz: a reconnaissance study. Earth Planet. Sci. Lett. 202, 709–724.
Müller, A., Herrington, R., Armstrong, R., Seltmann, R., Kirwin, D.J., Stenina, N.G., Kronz, A., 2010. Trace elements and cathodoluminescence of quartz in stockwork veins of Mongolian porphyry-style deposits. Mineral. Deposita 45, 707–727.
Müller, A., Wanvik, J.E., Ihlen, P.M., 2012. Petrological and chemical characterisation of high-purity quartz deposits with examples from Norway, Quartz: deposits, mineralogy and analytics. Springer, pp. 71–118.
Perny, B., Eberhardt, P., Ramseyer, K., Mullis, J., Pankrath, R., 1992. Microdistribution of Al, Li, and Na in α quartz: possible causes and correlation with short-lived cathodoluminescence. Am. Mineral. 77, 534–544.
Rice, C.M., Mark, D.F., Selby, D., Neilson, J.E., Davidheiser-Kroll, B., 2016. Age and geologic setting of quartz vein-hosted gold mineralization at Curraghinalt, Northern Ireland: implications for genesis and classification. Econ. Geol. 111, 127–150.
Rusk, B., 2009. Insights into hydrothermal processes from cathodoluminescence and trace elements in quartz, In: (editors), S.S.f.E.a.M.P.J.W.e.a. (Ed.), Proceedings of the Tenth Biennial SGA Meeting, Townsville.
Rusk, B., 2012. Cathodoluminescent textures and trace elements in hydrothermal quartz. In: Götze, J., Möckel, R. (Eds.), Quartz: Deposits. Mineralogy and Analytics. Springer, Berlin Heidelberg, Berlin, Heidelberg, pp. 307–329.
Rusk, B.G., Reed, M.H., Dilles, J.H., Kent, A.J.R., 2006. Intensity of quartz cathodoluminescence and trace-element content in quartz from the porphyry copper deposit at Butte, Montana. Am. Mineral. 91, 1300–1312.
Rusk, B.G., Lowers, H.A., Reed, M.H., 2008a. Trace elements in hydrothermal quartz: relationships to cathodoluminescent textures and insights into vein formation. Geology 36, 547–550.
Rusk, B.G., Reed, M.H., Dilles, J.H., 2008b. Fluid Inclusion evidence for magmatic-hydrothermal fluid evolution in the porphyry copper-molybdenum deposit at Butte, Montana. Econ. Geol. 103, 307–334.
Rusk, B., Koenig, A., Lowers, H., 2011. Visualizing trace element distribution in quartz using cathodoluminescence, electron microprobe, and laser ablation-inductively coupled plasma-mass spectrometry. Am. Mineral. 96, 703–708.
Seyedolali, A., Krinsley, D.H., Boggs Jr., S., O'Hara, P.F., Dypvik, H., Goles, G.G., 1997. Provenance interpretation of quartz by scanning electron microscope–cathodoluminescence fabric analysis. Geology 25, 787–790.
Sun, T., 2006. A new map showing the distribution of granites in South China and its explanatory notes. Geological Bulletin of China 25, 332–335.
Wilkinson, J.J., Boyce, A.J., Earls, G., Fallick, A.E., 1999. Gold remobilization by low-temperature brines; evidence from the Curraghinalt gold deposit, Northern Ireland. Econ. Geol. 94, 289–296.
Zhang G.Q., 2008. Geochemistry of hydrothermal uranium deposits in South China:A case study of the No.302 uranium deposit. Unpublished D.Sc. thesis, the University of Chinese Academy of Sciences, 1–127 (in Chinese with English abstract).
Zhang, C., Cai, Y., Xu, H., Dong, Q., Liu, J., Hao, R., 2017a. Mechanism of mineralization in the Changjiang uranium ore field, South China: evidence from fluid inclusions, hydrothermal alteration, and H–O isotopes. Ore Geol. Rev. 86, 225–253.
Zhang, L., Chen, Z., Li, S., Santosh, M., Huang, G., Tian, Z., 2017b. Isotope geochronology, geochemistry, and mineral chemistry of the U-bearing and barren granites from the Zhuguangshan complex, South China: implications for petrogenesis and uranium mineralization. Ore Geol. Rev. 91, 1040–1065.
Zhang, L., Chen, Z., Li, X., Li, S., Santosh, M., Huang, G., 2018. Zircon U-Pb geochronology and geochemistry of granites in the Zhuguangshan complex, South China: Implications for uranium mineralization. Lithos 308, 19–33.
Zhou, X.M., 2007. Genesis of the Late Mesozoic Granites at Nanling: Implications to Lithosphere Dynamic Evolution. Science Publishing House, Beijing (in Chinese).